Open charm as a probe of preequilibrium dynamics in nuclear collisions?

Ziwei Lin and Miklos Gyulassy
Department of Physics, Columbia University, New York, New York 10027
(Received 12 September 1994; revised manuscript received 20 December 1994)

The preequilibrium contribution to open charm production in nuclear collisions at $\sqrt{s} = 200A$ GeV is calculated using three different models for the correlations between momentum and space-time coordinates. Ideal (Bjorken) correlation between the rapidity y and space-time rapidity η of minijet gluons suppresses greatly the preequilibrium yield, and even allowing for the minimal uncertainty correlations leads, in contrast to previous estimates, only to a small preequilibrium charm yield as compared to the initial yield due to gluon fusion. The "intrinsic" charm process is negligible in the midrapidity domain.

PACS number(s): 25.75.+r, 24.85.+p

I. INTRODUCTION

Open charm, direct photon, and dilepton production are among the most direct probes [1–4] of the early time evolution of the quark-gluon plasma produced in ultrarelativistic nuclear reactions. At collider energies $\sqrt{s} > 200A$ GeV the initial minijet plasma is mostly gluonic [5, 6] with a quark content far below its chemical equilibrium value. Furthermore, the initial transverse momentum distribution of those gluons is very broad [2], resembling a hot thermal gas of gluons with an effective temperature $T \sim 500$ MeV [5]. Because charm is produced mainly through gluon fusion, open charm production provides a probe of that initial gluonic state. In contrast, hidden charm [7] is mostly sensitive to final state interactions in the later stages of evolution. Photons and dileptons are complementary probes of the evolution of the suppressed quark component of the plasma.

The present study is motivated by two recent studies [2, 4] of open charm which predicted widely different rates in nuclear collisions. In Ref. [2] the preequilibrium contribution was found to be almost equal to the initial gluon fusion rate. A similar factor of 2 enhancement of charm from thermal production in the hot-glue scenario was also suggested [5]. In Ref. [4], a more provocative claim was made that open charm may even be enhanced by over an order of magnitude above the initial perturbative QCD (pQCD) rate. The main result of our present study is that correlations between the rapidity y and the space-time rapidity η lead to a large suppression (about a factor of 40) relative to the uncorrelated case. Thus, preequilibrium open charm production is found to be unfortunately a very small fraction of the initial fusion rate. The large enhancement of charm production in Ref. [4] is found to be due to an overestimation of the contribution from flavor excitation processes and the use of a low energy A^α scaling from pp reactions measured at $E_{\rm lab} = 300$–400 GeV.

The paper is organized as follows: In Sec. II the dependence of the direct pQCD rates for charm production on structure functions, Q^2 scale, and K factor is reviewed and compared to existing data. The beam energy dependence and the A dependence of the initial charm production are compared to results in Ref. [4]. In Sec. III, the preequilibrium charm production is calculated. The minijet rapidity and transverse momentum distribution are fit to results of the Monte Carlo HIJING model [8] including initial and final state radiation. Three different models for the space-time and momentum correlations are studied and the influence on the charm yield is calculated. Of the three models, we concentrate on a minimally correlated model resulting from the uncertainty principle, which is similar to the type of correlation assumed in Ref. [9]. We also study the sensitivity of the results to different models of the formation physics [10]. Section IV contains the summary.

II. INITIAL CHARM PRODUCTION

Heavy-quark production in pp reactions was calculated in Ref. [11] including both fusion and heavy flavor excitation processes in leading-order pQCD. It was proposed that flavor excitation processes were dominant at high energies because a small Q^2 exchange can easily liberate any charm component in the nucleon while gluon fusion was suppressed because $Q^2 \geq 4M_c^2$. In the parton cascade model (PCM) [4], both mechanisms are incorporated to calculate s, c, b quark production in nuclear collisions. There the results suggested that the flavor excitation of the charm quark of nuclear structure functions would be the dominant source of charm production in nuclear collisions as well. However, it is pointed out [12] that the original flavor excitation rates in Ref. [11] were too high in the $x_f \sim 0$ region due to neglected interference with other pQCD amplitudes to the same order. When all diagrams were added together, a large destructive interference was found to suppress the flavor excitation rates by powers of Λ/M_q, where $\Lambda \sim 300$ MeV is a typical QCD scale and M_q is the heavy-quark mass. The suppression factor appears in the process $g + c(\bar{c})$ where charm is evolved from the structure functions using *perturbative* QCD, as also shown in Ref. [13]. We note that there is a possible nonperturbative charm component (intrinsic charm) in the nucleon. There are experimental constraints on the amount of that nonperturbative charm

component [14, 15]. The total contribution of the intrinsic charm was shown in Refs. [16, 17] to be small (about 10%) in the midrapity region where most of the charm is made. Although the contribution of the intrinsic charm component appears important at large x_f, its contribution to the total cross section is small and well within the uncertainties from other sources.

In this paper we only include fusion processes for the parton level cross sections as in Ref. [2]. For the production in p-p collisions, we use the light-quark and gluon structure functions from Glück *et al.* [18] and Duke and Owens [19] for comparison. The pQCD differential cross sections for $a+b \to c\bar{c}+X$ are taken from Ref. [11]. For example,

$$\sigma_{q\bar{q}\to c\bar{c}} = \frac{8\pi\alpha_s^2(Q^2)}{27\hat{s}^2}(\hat{s}+2M_c^2)\,\chi, \tag{1}$$

$$\sigma_{gg\to c\bar{c}} = \frac{\pi\alpha_s^2(Q^2)}{3\hat{s}}\left[-\left(7+\frac{31M_c^2}{\hat{s}}\right)\frac{1}{4}\chi + \left(1+\frac{4M_c^2}{\hat{s}}+\frac{M_c^4}{\hat{s}^2}\right)\ln\frac{1+\chi}{1-\chi}\right], \tag{2}$$

where $\chi = \sqrt{1-4M_c^2/\hat{s}}$ and we consider the following two choices for the scale Q^2 in the coupling constant $\alpha_s(Q^2) = 12\pi/\left[(33-2n_f)\ln(Q^2/\Lambda^2)\right]$ from Ref. [11]: (1) for $gg \to c\bar{c}, Q^2 = \hat{s}/2$, for $q\bar{q} \to c\bar{c}, Q^2 = \hat{s}$ [Q^2 choice (1)] and (2) for both $gg \to c\bar{c}$ and $q\bar{q} \to c\bar{c}, Q^2 = \hat{s}$ [Q^2 choice (2)].

We take $n_f = 4$ for charm quark production and $n_f = 5$ for bottom quark production. The QCD scale Λ depends on the choice of parton distribution functions and is given in Table I.

To incorporate approximately the next-to-leading-order corrections to the above rates we multiply the leading-order results by a K factor. In general, the K factor depends on the choice of parton distribution functions, the center of mass energy of the collision, and the type of projectile and target particles. Calculations to order $O(\alpha_s^3)$ for the subprocesses were carried out [20, 21], and afterwards calculations to order $O(\alpha_s^3)$ for $p+p$ collisions were made [22, 23]. For DO1, $M_c = 1.5$ GeV, $Q^2 = 4M_c^2$, and $P_{\rm lab} = 100$–1000 GeV, the K factor for p-p collisions [22] was found to range from 2.85 to 4.1. We also note a recent result [24] where the dependence of the K factor on the final momentum of the initially produced charm was studied for high energy AA collisions. As a function of the rapidity of the charm, the K factor is almost a constant ~ 2. As a function of $p_\perp$, the K factor increases from 1.3 at $p_\perp = 0.7$ GeV to 3.4 at $p_\perp = 6$ GeV.

TABLE I. QCD scale Λ for various choices of the parton distribution function.

Parton distribution functions	Λ (GeV)
GRV-LO set	0.25
GRV-HO set	0.20
Duke-Owens set 1 (DO1)	0.20
Duke-Owens set 2 (DO2)	0.40

In Fig. 1 we compare the so calculated charm cross section to the limited data on inclusive $c\bar{c}$ production in p-p collisions. The NA34 data for $\sigma_{\rm charm}$ are taken directly from Ref. [25]. The values for the other data lines are computed from D-meson cross sections according the argument in Ref. [26] by using the published experimental results [27–30]. Earlier experimental results [31] also show large uncertainties among the different experiments.

In Fig. 1 we see that both the solid curve and the dashed curve fit the low energy data reasonably well, and so we use these two parametrizations for the following high energy calculations in this section. As a consistency check, we also plot the long-dashed curve using the same parameters as in Fig. 1 of Ref. [22] (i.e., DO1, $M_c = 1.5$ GeV, $Q^2 = 4M_c^2$) using a constant $K = 3$ for simplicity. Comparing the solid and dot-dashed curves shows the strong dependence on the assumed charm quark mass for the GRV-HO set. Comparing the solid and dashed curves we see that different choices for the Q^2 scale can be compensated for by shifts in the K factor. These results together with the large uncertainty of the data emphasize the need to measure pp and pA to fix uncertainties in the initial charm production rate in order that charm production in AA can be properly calculated.

Next we compare our results for the rapidity density of produced $c\bar{c}$ pairs at $Y = 0$ with results of Ref. [4]. In Fig. 2 the energy dependence in the range between RHIC and LHC ($\sqrt{s} = 200$–$6300A$ GeV) for Au+Au collisions is shown. The scaling from pp results to AA is

$$\left(\frac{dN}{dY}\right)_{Y=0}^{AA} = A^{\alpha+1/3}\left(\frac{d\sigma}{dY}\right)_{Y=0}^{pp}\Big/\sigma_{\rm inelastic}^{pp}, \tag{3}$$

where $\sigma_{\rm inelastic}^{pp}$ is taken from Ref. [32]. Glauber geometry for central high $A+A$ collisions gives $\alpha = 1$. In Fig. 2 the solid curve is our result using the same parameters

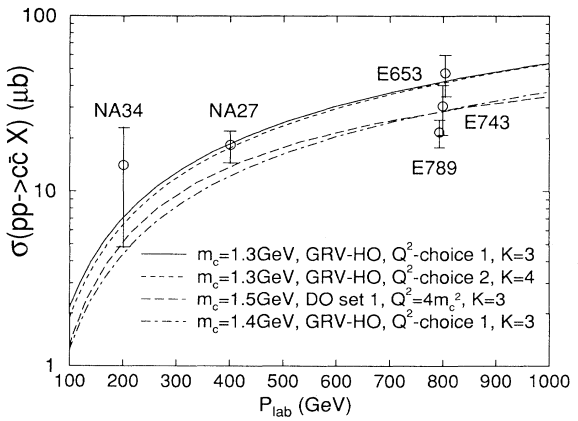

FIG. 1. The cross section for $pp \to c\bar{c}X$ is plotted as a function of $P_{\rm lab}$. The solid line is our result with $M_c = 1.3$ GeV, $K = 3$, Q^2 choice (1), and GRV-HO set. The long-dashed curve is the result with the same parameters as in Fig. 1 of [22], but using a K factor of 3 instead of doing an $O(\alpha_s^2)$ calculation.

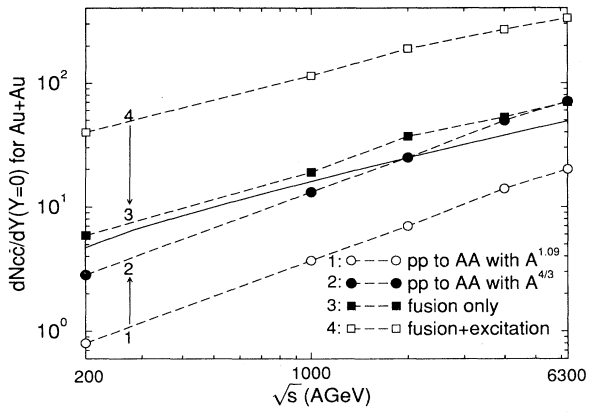

FIG. 2. $(dN_{c\bar{c}}/dY)_{Y=0}$, rapidity density of charm and anticharm pairs for Au-Au collisions vs $\sqrt{S}/A$. Curves 1–4 from the calculation of the parton cascade model [4] are compared to our calculation of the yield (the solid line) due to initial fusion processes. The top curve 4 is the total charm production with QGP formation including incoherent flavor excitation processes. Curve 3 shows the charm production in the case of QGP formation without excitation processes. The bottom curve 1 is the parton model result extrapolated to AA from pp using the $A^{0.76}$ scaling measured at much lower energies. Curve 2 is the parton model result scaled by $A^{4/3}$. Our curve uses the asymptotic $A^{4/3}$ scaling. As shown by the two arrows, curve 4 becomes curve 3 when the coherent cancellation of flavor excitation processes is considered, and curve 1 becomes curve 2 when high energy scaling is used. So the net dynamical enhancement in the PCM (by comparing curve 3 to curve 2) is comparable to the result of Ref. [2].

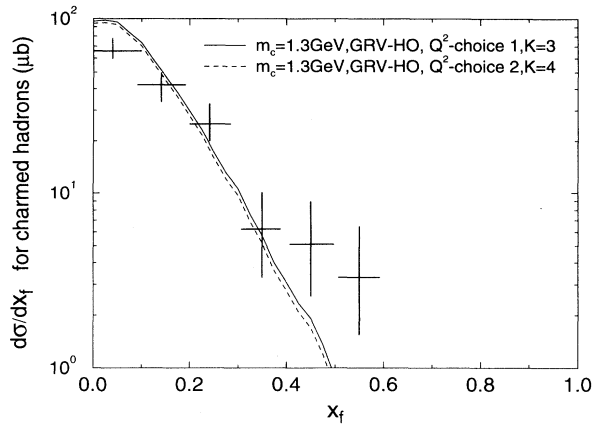

FIG. 3. The production of charmed hadrons as a function of x_f for p-p collisions at $P_{\rm lab} = 400$ GeV [27]. The solid curve is our result for $d\sigma/dx_f$ using the first parametrization. The dashed curve is our result using the second parametrization. These curves assume a delta function charm fragmentation function.

as for the solid curve in Fig. 1. The parametrization for the dashed curve in Fig. 1 gives a curve higher than the solid curve by 15%–30%. The four long-dashed curves, curve 1 to curve 4, are all from PCM calculations [4]. The top curve 4 is the parton cascade model result for the so-called quark-gluon plasma (QGP) formation case, including both fusion and the flavor excitation processes. That curve is higher than our solid curve by about an order of magnitude because it includes the contribution from flavor excitation processes. Curve 3, the curve with solid squares, shows the contribution to curve 4 from fusion processes only [processes (1) and (2) in the notation of Ref. [4]], and curve 3 is very close to our results. The bottom curve 1 is the estimate without QGP formation by extrapolating the parton model pp result to AA using $A^{1.09}$ scaling. It is lower than our solid curve by a factor of 6–2.5. The main source of this difference is from the A dependence of p-A cross sections. Reference [4] used an A^α scaling with $\alpha = 0.76$ [33] instead of the value $\alpha = 1$ we use from Glauber geometry. We note that the value $\alpha = 0.76$ is taken from low energy experiments, where energy conservation suppresses the contribution from multiple collisions. At high energies, QCD factorization implies that $\alpha = 1$ for p-A scaling is the appropriate scaling modulo small nuclear shadowing effects. To demonstrate this effect from different A^α scalings, we multiply curve 1 by a factor of $A^{1.0}/A^{0.76} = 3.55$ and get curve 2, which is close to our results. In summary, the factor ~ 50 enhancement of charm production suggested in Ref. [4] comparing curve 1 with curve 4 for charm production at RHIC is a consequence of the inclusion of incoherent flavor excitation processes and the extrapolation from pp to AA via low energy scaling. Given the coherent suppression of the flavor excitation processes [12] and the high energy scaling under consideration, it is only sensible to compare curve 2 with curve 3. In that case Fig. 2 leads to the expectation that preequilibrium charm production should be comparable to the initial fusion rate. This removes the bulk of the discrepancy between Ref. [2] and Ref. [4].

As a further check on the parameters we compare charmed hadron x_f results in Fig. 3 with 400 GeV p-p data [27] using the idealized δ-function fragmenta-

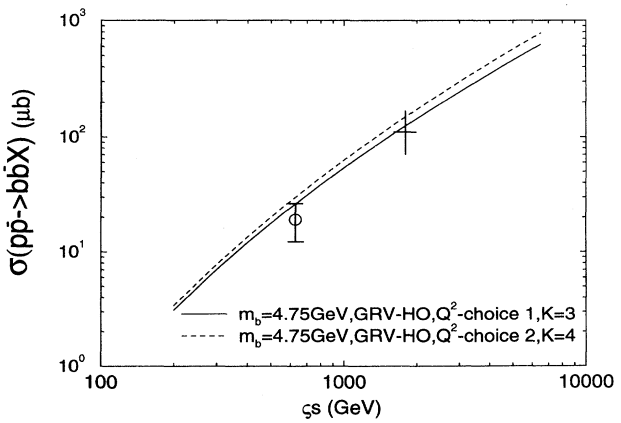

FIG. 4. The cross section for $p\bar{p} \to b\bar{b} + X$ vs $\sqrt{S}/A$. The data point at $\sqrt{S} = 630$ GeV is from Ref. [34]. The dashed cross at $\sqrt{S} = 1.8$ TeV is obtained indirectly from [23], and the error bar is only illustrative.

tion function. The realistic fragmentation function used in Ref. [16] lowers the curves slightly and reveals the true high-x_f intrinsic charm component. In Fig. 4 we compare $b\bar{b}$ production. Here we take $M_c = 4.75$ GeV as in Ref. [23], with $K = 3$, $n_f = 5$. The data point at $\sqrt{S} = 630$ GeV is from Ref. [34]: $\sigma(p\bar{p} \to b + X) = 19.3 \pm 7(\text{expt}) \pm 9(\text{theor})$ μb, and only the experimental error is indicated in Fig. 4. At $\sqrt{S} = 1.8$ TeV, our value is 41.8 μb $\times K = 125$ μb. This is significantly larger than found in Ref. [23].

III. PREEQUILIBRIUM CHARM PRODUCTION

We consider next the preequilibrium contribution to the charm yield in $A + A$. This is the charm produced through final state interactions between partons in the dense minijet plasma. Here we only calculate the dominant contribution from minijet gluon fusion.

A. Spectrum of minijets

The spectrum of minijet gluons in leading order follows from Ref. [35]:

$$\frac{d\hat{\sigma}}{d\hat{t}}_{gg\to gg} = \frac{9}{2}\frac{\pi\alpha_s^2}{\hat{s}^2}\left[3 - \frac{\hat{u}\hat{t}}{\hat{s}^2} - \frac{\hat{u}\hat{s}}{\hat{t}^2} - \frac{\hat{s}\hat{t}}{\hat{u}^2}\right], \tag{4}$$

$$\frac{d\hat{\sigma}}{d\hat{t}}_{gq\to gq} = \frac{\pi\alpha_s^2}{\hat{s}^2}\left[-\frac{4}{9}\frac{\hat{u}^2+\hat{s}^2}{\hat{u}\hat{s}} + \frac{\hat{u}^2+\hat{s}^2}{\hat{t}^2}\right]. \tag{5}$$

The term "minijets" refers to unresolved jets at a scale $p_\perp > p_{\perp\text{cut}} = 2$ GeV. The inclusive cross section to produce minijets is given by

$$\frac{d\sigma}{dydp_\perp^2} = \int dy_3 x_1 f_1 x_2 f_2 \frac{d\hat{\sigma}}{d\hat{t}}(1+2\to 3+4), \tag{6}$$

where f_1 is the incident parton distribution evaluated at $x_1 = p_\perp(e^y + e^{y_3})/\sqrt{s}$ at a scale $Q^2 = p_\perp^2$. The light-cone coordinates of the initial and final partons are $p_1 = [2x_1p_0, 0, \vec{0}]$, $p_2 = [0, 2x_2p_0, \vec{0}]$, $p_3 = [m_\perp e^{y_3}, m_\perp e^{-y_3}, -\vec{p}_\perp]$, and the observed parton has $p = [m_\perp e^y, m_\perp e^{-y}, \vec{p}_\perp]$. The subprocess Mandelstam variables are $\hat{s} = sx_1x_2$, etc. For the calculation of minijet gluon fusion process in the following Sec. III B, we choose $Q^2 = \hat{s}$. As in Ref. [2], we use DO1 as the proton structure functions and $K = 2$, $M_c = 1.5$ GeV for the minijet production. Shadowing on Au is taken from Ref. [36]. The resulting transverse momentum distribution of midrapidity minijet gluons at $\sqrt{s} = 200A$ GeV is shown by the open circles in Fig. 5. We call this distribution the hard distribution since it has $p_{\perp\text{cut}} = 2$ GeV. It is compared to the solid line, which is the output of the Monte Carlo calculation via the HIJING model [8] that includes initial and final state radiation.

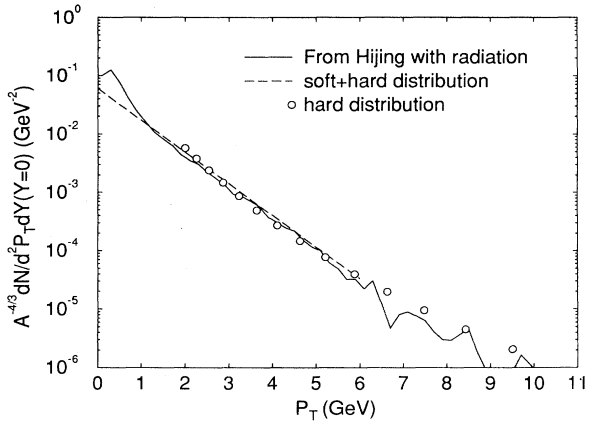

FIG. 5. The minijet gluon distribution $A^{-4/3}(dN/dyd\vec{p}_\perp)_{y=0}$ is plotted. The solid curve is taken from the HIJING calculation with radiation effects included, and the circles are our result from the initial production. The dashed line is the fit $0.06e^{-1.25p_\perp}$.

For convenience we have parametrized the Monte Carlo results as the following:

$$\frac{dN}{dyd\vec{p}_\perp} \equiv g(p_\perp)\rho(y)A^{4/3} = 0.06e^{-1.25p_\perp}\cos\left[\frac{\pi(\frac{y}{3.7})^{1.8}}{2}\right]A^{4/3} \quad \text{with } |y| \le 3.7. \tag{7}$$

In the following, we call this parametrized distribution the soft+hard distribution. The soft+hard, hard, and Monte Carlo distributions are very close to each other in the semihard $p_\perp > 2$ GeV region at $y = 0$, as seen in Fig. 5. However, the parametrized distribution falls underneath the Monte Carlo result in the region $p_\perp < 1$ GeV. We emphasize that the soft component is strongly model dependent as it requires the furthest extrapolation from the pQCD hard domain. The HIJING yield in that region is due to initial and final state radiation. Other contributions in this soft domain from coherent string are possible [6]. While most of the following results are obtained with the simple parametrization above, we will check the sensitivity to variations of the soft component as well. We also note that at larger rapidity the $p_\perp$ spectrum falls more rapidly. The above parametrization does not include that property. However, that property only lowers the high-$p_\perp$ tail, and hardly changes the low-$p_\perp$ part and the total number of the preequilibrium charm.

B. η-y correlations

1. *Bjorken correlation*

In ideal Bjorken dynamics, the space-time rapidity $\eta = \frac{1}{2}\ln[(t+z)/(t-z)]$ and the true momentum rapidity $y = \frac{1}{2}\ln[(E+p_z)/(E-p_z)]$ are assumed to be per-

fectly correlated. This is referred to as the inside-outside picture and the phase-space distribution function in this case has the form

$$F(\vec{x},\vec{p},t)_{Bj} = \frac{(2\pi)^3}{\tau\pi R_A^2 p_\perp}\frac{dN}{dyd\vec{p}_\perp} \times\delta(\eta-y)\Theta(\tau-\tau_i)\Theta(\tau_f-\tau). \quad (8)$$

$\tau_i = 0.1$ fm/c is the minijet formation time. $\tau_f \approx 1.7$ fm/c is the proper time when the energy density of the preequilibrium minijets falls by an order of magnitude to ~ 2 GeV/fm^3 due to rapid longitudinal expansion, and that is when we terminate the preequilibrium stage.

The phase-space distribution is normalized such that

$$\int \frac{F(\vec{x},\vec{p},t)_{Bj}d^3x}{(2\pi)^3} = \frac{d^3N}{d^3p} = \frac{1}{E}\frac{dN}{dyd\vec{p}_\perp}. \quad (9)$$

In this section we study the preequilibrium charm production at $y=0$ [2]:

$$\left(E\frac{d^3N}{d^3p}\right)_{y=0} = \int d^4x \int \frac{1}{32(2\pi)^8}\frac{d^3p_1 d^3p_2 d^3p'}{\omega_1\omega_2 E'} F(\vec{x},\vec{p}_1,t)\; F(\vec{x},\vec{p}_2,t)\; |M|^2\; \delta^{(4)}\left(\sum P^\mu\right). \quad (10)$$

Denoting $dN/dyd\vec{p}_\perp \equiv g(y,p_\perp)$ and $\vec{p}_{\perp_1} = (\cos\phi_1, \sin\phi_1, 0)p_{\perp 1}$, the ideal η-y correlation leads to

$$\left(E\frac{d^3N}{d^3p}\right)_{y=0} = \int_{\tau_i}^{\tau_f}\frac{d\tau}{32(2\pi)^2\tau\pi R_A^2}\int d\eta dp_{\perp 1}dp_{\perp 2}d\phi_1 d\phi_2 \frac{g(\eta,p_{\perp 1})g(\eta,p_{\perp 2})\delta(\sum E)|M|^2}{E'}$$

$$= \frac{\ln(\tau_f/\tau_i)}{32(2\pi)^2\pi R_A^2}\int d\eta dp_{\perp 2}d\phi_1 d\phi_2 \frac{g(\eta,p_{\perp 1,0})g(\eta,p_{\perp 2})|M|^2}{p_{\perp 2}[1-\cos(\phi_1-\phi_2)] - (E\cosh\eta - p\cos\phi_1)}. \quad (11)$$

In deriving the above, we have used kinematic relations

$$E' = (p_{\perp 1}+p_{\perp 2})\cosh\eta - E,$$

$$\frac{\delta(\sum E)}{E'} = \frac{\delta(p_{\perp 1}-p_{\perp 1,0})}{p_{\perp 2}[1-\cos(\phi_1-\phi_2)] - (E\cosh\eta - p\cos\phi_1)},$$

$$p_{\perp 1,0} = \frac{p_{\perp 2}(E\cosh\eta - p\cos\phi_2)}{p_{\perp 2}[1-\cos(\phi_1-\phi_2)] - (E\cosh\eta - p\cos\phi_1)}. \quad (12)$$

Numerical integration of the above integral in Eq. (11) leads to the results shown in Fig. 6. The solid line is the $p_\perp$ distribution for the initial charm production, from Sec. II. We see that the preequilibrium contribution in this strongly correlated case is totally negligible. This result is similar to the thermal charm production contribution calculated in Ref. [2] except that in our case the curve extends to higher $p_\perp$ because of the broader initial minijet distribution in $p_\perp$.

2. *Uncorrelated η-y*

In Ref. [2], another extreme case, opposite to the ideal Bjorken picture, was considered. In that case the gluon distribution is assumed to be completely uncorrelated as in an ideal thermal fireball. This assumption leads to

$$F(\vec{x},\vec{p},t)_{\rm FB} = \frac{(2\pi)^3}{p}\frac{1}{V}\frac{dN}{dyd\vec{p}_\perp}. \quad (13)$$

If one assumes a fixed volume $V = \tau_i\pi R_A^2$, then $\int dt \sim \tau_f - \tau_i$, and

$$\int \frac{d^4x}{V^2} \sim \frac{1}{\pi R_A^2}\frac{\tau_f}{\tau_i} \quad (14)$$

as in Ref. [2]. Then from Eq. (10), we have

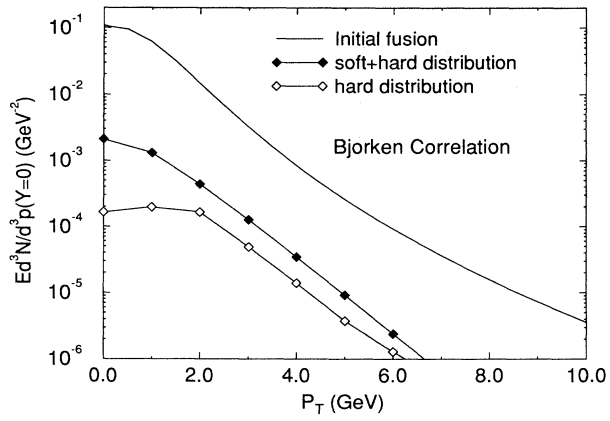

FIG. 6. The distribution $\left(Ed^3N/d^3p\right)_{y=0}$ of charm quark production using $\delta(\eta-y)$ correlation is plotted as a function of $p_\perp$. The solid curve is the initial charm production. The curve labeled with solid diamonds is the preequilibrium contribution including both the soft ($p_\perp < 2$ GeV) and hard ($p_\perp > 2$ GeV) components of the minijet gluons. The curve labeled with open diamonds is the preequilibrium contribution including only the hard component.

$$\left(E\frac{d^3N}{d^3p}\right)_{y=0} = \frac{I(p_\perp)}{32(2\pi)^2}\int\frac{d^4x}{V^2} = \frac{\tau_f/\tau_i}{32(2\pi)^2\pi R_A^2}I(p_\perp), \tag{15}$$

where

$$I(p_\perp) = \int dy_1 dy_2 dp_{\perp 2} d\phi_1 d\phi_2 \frac{g(y_1,p_{\perp 1,0})g(y_2,p_{\perp 2})|M|^2}{p_{\perp 2}\left[\cosh(y_1-y_2)-\cos(\phi_1-\phi_2)\right]-(E\cosh y_1 - p\cos\phi_1)},$$

$$\frac{\delta\left(\sum E\right)}{E'} = \frac{\delta(p_{\perp 1}-p_{\perp 1,0})}{p_{\perp 2}\left[\cosh(y_1-y_2)-\cos(\phi_1-\phi_2)\right]-(E\cosh y_1 - p\cos\phi_1)},$$

$$p_{\perp 1,0} = \frac{p_{\perp 2}(E\cosh y_2 - p\cos\phi_2)}{p_{\perp 2}\left[\cosh(y_1-y_2)-\cos(\phi_1-\phi_2)\right]-(E\cosh y_1 - p\cos\phi_1)}. \tag{16}$$

For the uncorrelated case, the preequilibrium charm production is much larger than the Bjorken correlation case, and is comparable with the initial charm yield, as shown in Fig. 7. This is similar to the result in Ref. [2] where preequilibrium charm production has almost the same magnitude and $p_\perp$ shape as the initial charm.

3. *Minimally correlated η-y*

We consider here the simplest source of η-y correlations resulting from the minimal geometrical spread in initial production points required by the uncertainty principle. These type of correlations are included in the parton cascade model and discussed in Ref. [9]. The phase-space distribution function including such minimal correlations has the form

$$F(\vec{x},\vec{p},t)_{\min} = \mathcal{N}\int\frac{dN}{dyd\vec{p}_\perp}\frac{\theta(\tau_{\max}-\frac{t}{\cosh y})}{1+(\frac{t_f(p)}{\Delta t})^2}\rho_0(\vec{x_0},t_0)\delta(\vec{x}-\vec{x_0}-\vec{v}\Delta t)d^3x_0dt_0. \tag{17}$$

The integration is over the space-time coordinates $(\vec{x}_0,t_0)$ of the production points of the gluons. These points are distributed according to a normalized density $\rho_0(\vec{x}_0,t_0)$. The delta function arises to take into account the free streaming of the partons from the production point, with velocity $\vec{v}=\vec{p}/E$, where $E = p_\perp\cosh y$ and $p_z = p_\perp\sinh y$. The theta function defines what we mean by preequilibrium. The proper time when the preequilibrium fusion is terminated is $\tau_{\max}$, which is determined in Fig. 8. The theta function ensures that only those gluons with proper time less than $\tau_{\max}$ contribute.

The formation physics is included via the Lorentzian formation factor [10]

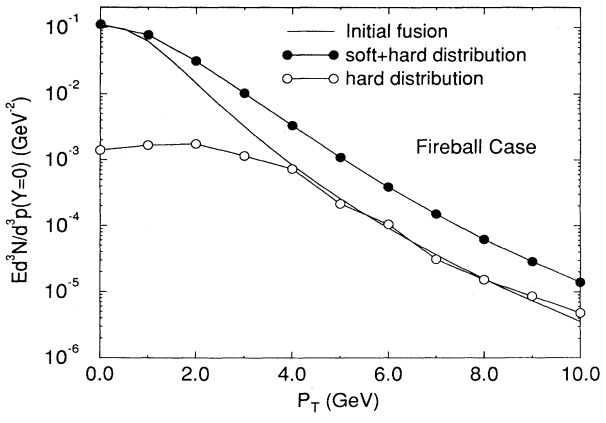

FIG. 7. The distribution $\left(Ed^3N/d^3p\right)_{y=0}$ of charm quark production for the uncorrelated case is plotted as a function of $p_\perp$. The solid curve is the initial charm production. The curve labeled with solid circles is the preequilibrium contribution including both the soft ($p_\perp < 2$ GeV) and hard ($p_\perp > 2$ GeV) components. The curve labeled with open circles is the preequilibrium contribution including only the hard component.

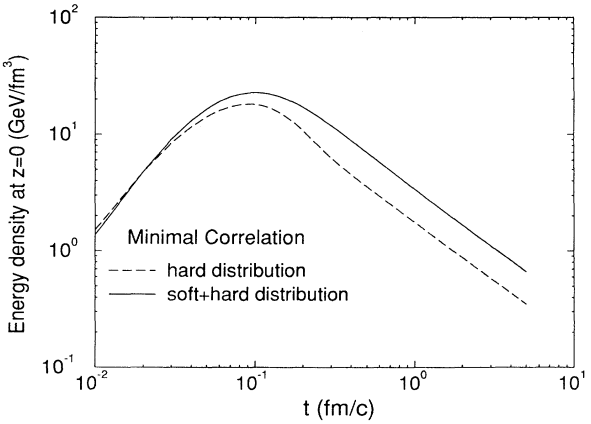

FIG. 8. The energy density at $z = 0$ is plotted as a function of proper time assuming minimal correlations and Lorentzian formation probability. The solid curve includes both soft and hard components while the dashed curve is calculated using the hard distribution and includes only the hard component.

$$[1+(t_f(p)/\Delta t)^2]^{-1} \ , \tag{18}$$

where $\Delta t = t - t_0$ is the elapsed time, and the formation time is given by

$$t_f(p) \simeq \cosh y \frac{0.2 \text{ GeV}}{p_\perp} \text{ (fm)} \ . \tag{19}$$

We note that the above formation factor more accurately describes the interference phenomena suppressing production at early time than the conventionally assumed factor

$$\theta[\Delta t - t_f(p)] \ . \tag{20}$$

In the following we consider both formation functions for comparison to check for the sensitivity to this formation physics.

We assume that $\int \rho_0(\vec{x_0}, t_0) d^3x_0 dt_0 = 1$. In this case the normalization factor is $\mathcal{N} = (2\pi)^3/E$, so that

$$\lim_{t\to\infty} \int F(\vec{x},\vec{p},t)_{\min} d^3x/(2\pi)^3 = d^3N/d^3p \ . \tag{21}$$

As discussed in Ref. [9], the production points are spread along the beam axis according to the uncertainty principle by an amount $\delta z \equiv d \sim \hbar/p_\perp$ since the dominant parton interaction leading to a $y = 0$ parton with final $p_\perp$ has an initial longitudinal momentum $xP_0 \sim p_\perp$. We take as a particular model

$$d = \frac{0.2}{p_\perp} \text{ (fm)}. \tag{22}$$

Clearly this is only a rough guess, but it allows us at least to investigate the sensitivity of the results to a particular η-y correlation that results from this spatial spreading of the production points. We emphasize that it is precisely the uncertainty of the initial space-time formation physics that leads us to study the possibility of open charm production as an experimental probe of that physics.

Given the above assumption we take

$$\rho_0(\vec{x_0}, t_0) = \frac{1}{\pi R_A^2} \delta(t_0) \frac{e^{-z_0^2/(2d^2)}}{\sqrt{2\pi} d}, \tag{23}$$

where d is the mean spread for gluons depending on $p_\perp$ from above. This distribution only spreads out the production points along the beam axis. A more realistic treatment would also smear out in the time coordinate.

Neglecting transverse expansion, we obtain finally

$$F(\vec{x},\vec{p},t)_{\min} = \frac{(2\pi)^3}{\sqrt{2\pi}\pi R_A^2} \frac{p_\perp}{0.2} e^{-(z-\tanh y\, t)^2 (\frac{p_\perp}{0.2})^2/2} \frac{1}{p} \frac{dN}{dy\, d\vec{p}_\perp} \frac{\theta(\tau_{\max} - \frac{t}{\cosh y})}{1+(\frac{0.2\cosh y}{p_\perp t})^2}. \tag{24}$$

Let $a_1 = \tanh y_1$, $a_2 = \tanh y_2$, $b_1 = (\frac{p_{\perp 1,0}}{0.2})^2/2$, $b_2 = (\frac{p_{\perp 2}}{0.2})^2/2$; then after integration over z, we have the final expression as the following, while its numerical results are shown in Fig. 9:

$$\left(E\frac{d^3N}{d^3p}\right)_{y=0} = \frac{\sqrt{\pi}}{16(2\pi)^4 R_A^2} \int dy_2 dy_1 dp_{\perp 2} d\phi_2 d\phi_1 \frac{p_{\perp 1,0} \frac{p_{\perp 1,0}}{0.2} \frac{p_{\perp 2}}{0.2} |M|^2}{p_{\perp 2} \cosh y_1 \cosh y_2 (E\cosh y_2 - p\cos\phi_2)}$$
$$\times \frac{g(y_1, p_{\perp 1,0}) g(y_2, p_{\perp 2})}{\sqrt{b_1+b_2}} \int_0^{t_f} dt \frac{e^{\frac{-(a_1-a_2)^2 t^2}{1/b_1+1/b_2}}}{\left[1+(\frac{0.2\cosh y_1}{p_{\perp 1,0} t})^2\right]\left[1+(\frac{0.2\cosh y_2}{p_{\perp 2} t})^2\right]}. \tag{25}$$

In the above $t_f = \tau_{\max} \min(\cosh y_1, \cosh y_2)$, and $p_{\perp 1,0}$ is the same as in Eq. (16). Note that by using the unit GeV for momentum and unit fm for time, the expression $\left(E\frac{d^3N}{d^3p}\right)_{y=0}$ in Eqs. (11), (15), and (25) has the dimension $\text{GeV}^{-4}\,\text{fm}^{-2}$, and we need a factor $(\hbar c)^2 \sim (0.2 \text{ GeV fm})^2$ to convert it to the dimension GeV^{-2}, which we have used in Figs. 6, 7, 9, and 10.

We also plot the energy density curve at $z = 0$ as a function of time in Fig. 8. We see that it increases first, and reaches a maximum at a time of about 0.1 fm/c; then the energy density decreases linearly to ~ 2 GeV/fm^3 at ~ 0.9 fm/c (1.7 fm/c) for hard (soft+hard) distribution. We choose the above time as the cutoff $\tau_{\max}$.

The previous uncorrelated case neglects the finite formation times of the minijets. In order to see the formation-time effect, we also use the θ-function form in Eq. (20) instead of the Lorentzian form in Eq. (18) for the formation-time effect. The result from this θ function is about 10% higher at $p_\perp = 0$ GeV, and 10% lower at $p_\perp = 9$ GeV, as shown in Fig. 10. The lack of sensitivity to the formation-time physics is due to the relative large $p_\perp$ for the gluon minijets in the charm production process. There would be more sensitivity had the production been dominated by low-$p_\perp$ components.

We also see that for the soft+hard distribution the soft gluons significantly increase the preequilibrium charm production in both the low-$p_\perp$ and high-$p_\perp$ regions, with the largest increase in low-$p_\perp$ region. It is interesting to identify where the enhancement comes from. In Fig. 9, the curve with diamonds shows the contribution from the fusion of soft gluons both with $p_\perp < 2$ GeV, and the curve

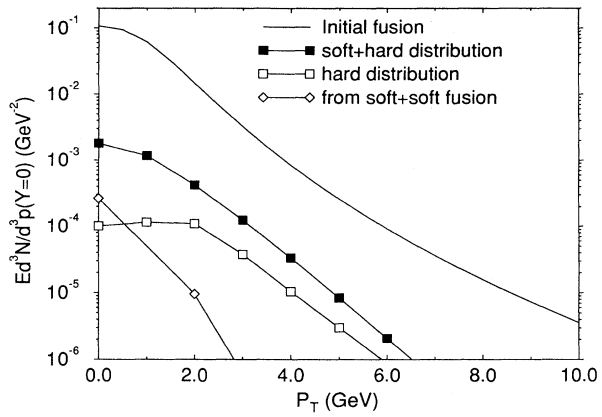

FIG. 9. The distribution $\left(Ed^3N/d^3p\right)_{y=0}$ of charm quark production using minimal η-y correlations is plotted as a function of $p_\perp$. The curve labeled with solid squares includes both components while that labeled with open squares includes only the fusion of hard gluons. The curve labeled with diamonds shows the contribution from fusion of soft gluons both with $p_\perp < 2$ GeV. This shows that the preequilibrium contribution mainly comes from the fusion of soft and hard gluons.

with open squares shows the contribution from the fusion of hard gluons both with $p_\perp > 2$ GeV. These two curves are both very low compared with the curve calculated from the soft+hard distribution. So the enhancement going from a hard distribution to a soft+hard distribution mainly comes from the fusion of hard and soft minijet gluons.

We have noted before that our fit for the minijet gluon spectrum falls below the Monte Carlo result from the HIJING calculation. We can fit the soft gluons from HIJING better by using $0.265e^{-2.6p_\perp}$ for $p_\perp \in (0, 1.1)$ GeV, and use the old fit $0.06e^{-1.25p_\perp}$ for higher-$p_\perp$ gluons. This new fit gives us more very soft gluons. We have done the calculation for the minimally correlated case using the new fit, and the result is different only by less than 10%, which means the supersoft gluons are not very important for preequilibrium charm production.

There is also a possible cross-term contribution from the interactions of the incoming nuclei and the preequilibrium gluon minijets. However, our preliminary result shows that it is not larger than the above preequilibrium charm yield and is therefore also negligible compared with the initial charm production.

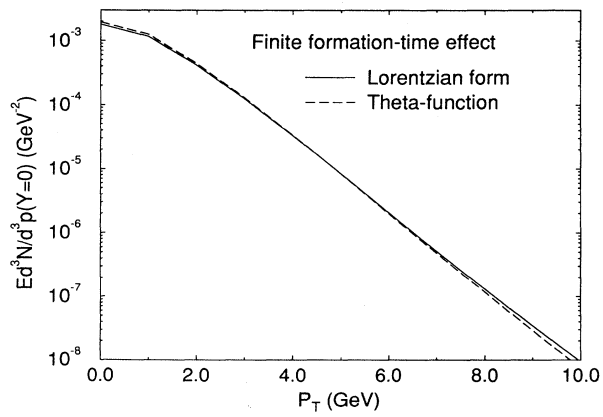

FIG. 10. The distribution $\left(Ed^3N/d^3p\right)_{y=0}$ of charm quark production using different formation-time probability distributions. The solid curve is obtained using the Lorentzian form in Eq. (18), and the dashed curve using the theta function form in Eq. (20).

C. Why is the preequilibrium charm yield so small?

To understand the reason why the preequilibrium charm yield is so small compared to the initial yield as found through tedious numerical calculations in the previous section, we consider here the calculation of the total number of preequilibrium charm pairs. The expression for that number is given by

$$N = \frac{(\hbar c)^2}{4(2\pi)^6}\int d^4x \int \frac{d^3p_1}{\omega_1}\frac{d^3p_2}{\omega_2} F(\vec{x},\vec{p}_1,t) \times F(\vec{x},\vec{p}_2,t)\hat{s}\hat{\sigma}(\hat{s}), \tag{26}$$

where $\hat{\sigma}(\hat{s})$ is the integrated cross section for the process $gg \to c\bar{c}$; see Eq. (2). Our main strategy is to estimate the mean difference between the two gluon rapidities and then from the kinematical constraint on charm production ($\hat{s} \geq 4M_c^2$) estimate the effective lower cutoff for $p_\perp$ of the minijet gluons. Thus we separate the $p_\perp$ integrals from the rapidity integrals and have a rough estimate for the total number of charm pairs.

1. Bjorken correlation case and uncorrelated case

For the fireball case,

$$F(\vec{x},\vec{p},t)_{\rm FB} = \frac{(2\pi)^3}{p}\frac{1}{V}\frac{dN}{dyd\vec{p}_\perp},$$

$$\hat{s} = 2p_{\perp 1}p_{\perp 2}\left[\cosh(y_1-y_2) - \cos(\phi_1-\phi_2)\right]. \tag{27}$$

For the Bjorken case,

$$F(\vec{x},\vec{p},t)_{\rm Bj} = \frac{(2\pi)^3}{p_\perp}\frac{dN}{dyd\vec{p}_\perp}\frac{\delta(\eta-y)}{\tau\pi R_A^2}\Theta(\tau-\tau_i)\Theta(\tau_f-\tau),$$

$$\hat{s} = 2p_{\perp 1}p_{\perp 2}\left[1-\cos(\phi_1-\phi_2)\right]. \tag{28}$$

For all the cases, we use the fit to the gluon distribution given by Eq. (7), where $g(p_\perp) \equiv ae^{-bp_\perp} = 0.06e^{-1.25p_\perp}$. Therefore,

$$N_{\rm FB} = \frac{(\hbar c)^2 \frac{\tau_f}{\tau_i} A^{8/3}}{4\pi R_A^2} \int dy_1 \frac{\rho(y_1)}{\cosh y_1} \int dy_2 \frac{\rho(y_2)}{\cosh y_2} \int dp_{\perp 1} g(p_{\perp 1}) \int dp_{\perp 2} g(p_{\perp 2}) \int d\phi_1 \int d\phi_2 \hat{s}\hat{\sigma}(\hat{s}),$$
$$N_{\rm Bj} = \frac{(\hbar c)^2 \ln \frac{\tau_f}{\tau_i} A^{8/3}}{4\pi R_A^2} \int d\eta \left[\rho(\eta)\right]^2 \int dp_{\perp 1} g(p_{\perp 1}) \int dp_{\perp 2} g(p_{\perp 2}) \int d\phi_1 \int d\phi_2 \hat{s}\hat{\sigma}(\hat{s}). \tag{29}$$

The dominant contribution is coming from the vicinity of the production threshold where $\hat{s} = 4M_c^2 = 9$ GeV^2 [11], and so we make the following rough estimates:

$$\hat{s}\hat{\sigma}(\hat{s}) \sim \alpha^2(\hat{s}) \sim 0.06\ ,$$
$$\int dp_\perp g(p_\perp) \sim \int_{p_c}^{\infty} dp_\perp g(p_\perp) \sim \frac{a}{be^{bp_c}}, \tag{30}$$

where p_c is the effective cutoff value for $p_{\perp 1}$ and $p_{\perp 2}$ from the requirement $\hat{s} \geq 4M_c^2$.

For the fireball case,

$$\langle \cosh(y_1 - y_2) \rangle \equiv \frac{\int dy_1 dy_2 \frac{\rho(y_1)}{\cosh y_1} \frac{\rho(y_2)}{\cosh y_2} \cosh(y_1 - y_2)}{\int dy_1 dy_2 \frac{\rho(y_1)}{\cosh y_1} \frac{\rho(y_2)}{\cosh y_2}} \sim 4.0. \tag{31}$$

Since the minijet $p_\perp$ spectrum is dropping almost exponentially, the production heavily favors the smaller cutoff p_c, and so the mean value of $\cos(\phi_1 - \phi_2)$ is most likely to be negative. We take $\langle \cos(\phi_1 - \phi_2) \rangle \sim -0.5$. Then $\hat{s} \sim 9p_c^2$, and so the effective cutoff for the fireball case is $p_c \sim 1.0$ GeV.

On the other hand, for the Bjorken case,

$$y_1 = y_2 = \eta \ \Rightarrow \hat{s} \sim 3p_c^2 \ \Rightarrow p_c \sim 1.73 \text{ GeV}. \tag{32}$$

Using the same values as in Sec. III B, $\tau_i = 0.1$ fm, $\tau_f = 1.0$ fm for the fireball case, $\tau_f' = 1.7$ fm for the Bjorken case, and

$$\int dy_1 \frac{\rho(y_1)}{\cosh y_1} \sim 2.8, \quad \int d\eta \left[\rho(\eta)\right]^2 \sim 4.9. \tag{33}$$

We then have the estimate for the total number of the preequilibrium charm:

$$N_{\rm FB} \sim \frac{(\hbar c)^2 \frac{\tau_f}{\tau_i} A^{8/3}}{4\pi R_A^2} 2.8^2 \left(\frac{a}{be^{1.0b}}\right)^2 (2\pi)^2 \left[\hat{s}\hat{\sigma}(\hat{s})\right] \sim 3.5,$$
$$N_{\rm Bj} \sim \frac{(\hbar c)^2 \ln \frac{\tau_f'}{\tau_i} A^{8/3}}{4\pi R_A^2} 4.9 \left(\frac{a}{be^{1.73b}}\right)^2 (2\pi)^2 \left[\hat{s}\hat{\sigma}(\hat{s})\right] \sim 0.098. \tag{34}$$

Therefore we estimate $N_{\rm FB}/N_{\rm Bj} \sim 35$, in rough agreement with the detailed numerics. We see that the main source of the large increase going from the Bjorken case to the fireball case comes from the different $p_\perp$ cutoff. In the uncorrelated fireball case, one allows particles with different rapidities to interact with each other [see Eq. (31)]; thus more low-$p_\perp$ gluons can take part in the interaction. Since the minijet $p_\perp$ spectrum is dropping almost exponentially, the fireball case produces a lot more preequilibrium charm than the Bjorken case (a factor of 6 increase from the smaller $p_\perp$ cutoff). Although the questionable linear proper time dependence in the fireball case also gives an considerable increase (about a factor of 3.5), it is not as important as the correlation effect.

2. *Minimal correlation case*

For the minimal correlation case, the estimate is unfortunately not as straightforward. The phase-space distribution function is

$$F(\vec{x}, \vec{p}, t)_{\rm min} = \frac{(2\pi)^3}{\sqrt{2\pi}\pi R_A^2} \frac{e^{-(z - \tanh y\, t)^2 (\frac{p_\perp}{\hbar c})^2/2}}{\hbar c \cosh y} \frac{dN}{dy\, d\vec{p}_\perp} \theta\left(\tau_{\rm max} - \frac{t}{\cosh y}\right) \theta\left(\frac{\hbar c \cosh y}{p_\perp} - \tau_{\rm max}\right) \tag{35}$$

and $\hat{s}$ is the same as in Eq. (27). In the above distribution function we choose to use the θ function for the formation-time effect. We have seen from Fig. 10 that Lorentzian formation-time formula and θ-function formula give almost the same result.

Using Eq. (26) and after the integration over z, we have

$$N_{\rm min} = \frac{(\hbar c)^2 A^{8/3}}{4\pi R_A^2 \sqrt{\pi}} \int dp_{\perp 1} g(p_{\perp 1}) \int dp_{\perp 2} g(p_{\perp 2}) \int d\phi_1 \int d\phi_2$$
$$\times \int dy_1 \frac{\rho(y_1)}{\cosh y_1} \int dy_2 \frac{\rho(y_2)}{\cosh y_2} \hat{s}\hat{\sigma}(\hat{s}) \int_{t_{\rm min}}^{t_{\rm max}} dt \frac{e^{\frac{-(a_1 - a_2)^2 t^2}{1/b_1 + 1/b_2}}}{\sqrt{1/b_1 + 1/b_2}}, \tag{36}$$

where

$$t_{\rm min} = \hbar c \max\left(\frac{\cosh y_1}{p_{\perp 1}}, \frac{\cosh y_2}{p_{\perp 2}}\right), \ t_{\rm max} = \tau_f \min(\cosh y_1, \cosh y_2), \tag{37}$$

and a_1, a_2, b_1, b_2 are defined the same as in Eq. (24).

We estimate that for the dominant part of the integral

$$\frac{1}{b_1}+\frac{1}{b_2}\sim\left(\frac{2\hbar c}{p_c}\right)^2,\ t_{\min}\sim\frac{\hbar c\cosh\bar{y}}{p_c},\ t_{\max}\sim\tau_f\cosh\bar{y}, \tag{38}$$

where $\bar{y}=(|y_1|+|y_2|)/2$. Now let $u=t\,p_c/(\hbar c\cosh\bar{y})$; then the last three-dimensional integral in Eq. (36) without the factor $\hat{s}\hat{\sigma}(\hat{s})$ is

$$J\sim\int dy_1\frac{\rho(y_1)}{\cosh y_1}\int dy_2\frac{\rho(y_2)}{\cosh y_2}\frac{1}{2}\cosh\bar{y}\int_1^{\frac{\tau_f p_c}{\hbar c}}du\,e^{-[\frac{\sinh(y_1-y_2)\cosh\bar{y}}{2\cosh y_1\cosh y_2}]^2u^2}. \tag{39}$$

The u integral gives a dependence on τ_f which is similar to the logarithmic dependence in the Bjorken case, and the exponential form in the integrand forces the spread y_1-y_2 to be small. Numerically, by taking $\tau_f\sim 1.7$ fm/c, $p_c\sim 2.0$ GeV (as the first-step value) in the u integral, the above three-dimensional integral is $J\sim 19.1$, and when the integrand is weighed by $\cosh(y_1-y_2)$, the integral is ~ 23.3. So

$$\langle\cosh(y_1-y_2)\rangle\sim 23.3/19.1\sim 1.22\Rightarrow\hat{s}\sim 3.44p_c^2\Rightarrow p_c\sim 1.62\ \text{GeV}. \tag{40}$$

Note that the above determined value of p_c is insensitive to the first-step p_c value we tried in the u integral.

Therefore for the total preequilibrium charm number

$$N_{\min}\sim\frac{(\hbar c)^2A^{8/3}}{4\pi R_A^2\sqrt{\pi}}\int dp_{\perp 1}g(p_{\perp 1})\int dp_{\perp 2}g(p_{\perp 2})\int d\phi_1\int d\phi_2\,J\,\hat{s}\hat{\sigma}(\hat{s})$$

$$\sim\frac{(\hbar c)^2A^{8/3}}{4\pi R_A^2}\frac{J}{\sqrt{\pi}}\left(\frac{a}{be^{1.62b}}\right)^2(2\pi)^2[\hat{s}\hat{\sigma}(\hat{s})]\sim 0.10. \tag{41}$$

Therefore $N_{\min}/N_{\rm Bj}\sim 1$. From the above estimate we can see that although the minimally correlated case allows particles with different rapidities to interact, the dominant contribution still comes from the region where the two gluons have almost the same rapidity; thus there is no sizable enhancement in the preequilibrium charm yield. The minimally correlated case is very much like the Bjorken case in that the dominant contribution comes from $y_1\simeq y_2$ region.

As a comparison to the above rough estimates in this section, the numerical integration gives $N_{\rm FB}=3.8$, $N_{\rm Bj}=0.093$, and $N_{\min}=0.078$, and so $N_{\min}/N_{\rm Bj}\sim 80\%$.

IV. DISCUSSION AND SUMMARY

In this paper, we calculated initial and preequilibrium charm production in nuclear collisions to test the sensitivity of this probe to the unknown initial conditions in such reactions. For the initial charm production, the sensitive dependence on the choice of structure functions, the Q^2 scale, and the K factor was noted. The parameters were fixed by fitting the limited available experimental data at lower energies. We emphasized the need for new measurements of pp and pA charm production to reduce the present large theoretical uncertainties. We argued that the copious charm production predicted in Ref. [4] was mainly due to the neglect of the coherent suppression of flavor excitation processes. Our calculated initial charm yields are close to those computed in Ref. [2] and to curve 2 in Fig. 2 from Ref. [4].

For the contribution from preequilibrium charm production, we studied the effect of correlations between the rapidity y and space-time rapidity η of minijet gluons. For the ideal Bjorken-correlated case, where $\eta=y_1=y_2$, the preequilibrium charm production is negligible compared with the yield due to initial gluon fusion. For the opposite extreme fireball case, corresponding to uncorrelated y and η, the preequilibrium charm production is almost a factor of 50 larger than in the Bjorken-correlated case and is comparable with the initial charm yield [2]. By the estimates of the total preequilibrium charm number, we found the the difference mainly comes from the η-y correlation. Therefore, the preequilibrium charm production is very sensitive to the (η-y) correlations in the initial state.

In order to investigate the effect of more realistic correlations that may exist in the initial minijet plasma, we introduced a minimal correlation model taking into account the uncertainty principle along the lines of Ref. [9]. Our main result is that this minimal correlation is similar to the ideal Bjorken correlation case and produces negligible preequilibrium charm compared with the initial charm yield. We also found that the preequilibrium charm yield is rather insensitive to the formation physics because the early-formed $p_\perp>1$ GeV gluons dominate.

ACKNOWLEDGMENTS

We thank K. Geiger, B. Müller, X.N. Wang, and L. Xiong for useful discussions and A. Mueller for bringing Refs. [12, 17] to our attention. This work was supported by the Director, Office of Energy Research, Division of Nuclear Physics of the Office of High Energy and Nuclear Physics of the U.S. Department of Energy under Contract No. DE-FG02-93ER40764.

[1] E. V. Shuryak, Phys. Lett. **78B**, 150 (1978).
[2] B. Müller and X. N. Wang, Phys. Rev. Lett. **68**, 2437 (1992).
[3] E. Shuryak and L. Xiong, Phys. Rev. Lett. **70**, 2241 (1993).
[4] K. Geiger, Phys. Rev. D **48**, 4129 (1993).
[5] E. Shuryak, Phys. Rev. Lett. **68**, 3270 (1992).
[6] K. J. Eskola and M. Gyulassy, Phys. Rev. C **47**, 2329 (1993); M. Gyulassy, K. J. Eskola, A. V. Selikhov, and X. N. Wang, in *CCAST Symposium Proceedings*, edited by Y. Pang, J. Qiu, and Z. Qiu (Gordon and Breach, Amsterdam, 1994), Vol. 10, p. 393.
[7] T. Matsui and H. Satz, Phys. Lett. B **178**, 416 (1986); S. Gavin, H. Satz, R. L. Thews, and R. Vogt, Z. Phys. C **61**, 351 (1994).
[8] X. N. Wang and M. Gyulassy, Phys. Rev. D **44**, 3501 (1991); **45**, 844 (1992).
[9] K. Geiger and B. Müller, Nucl. Phys. **B369**, 600 (1992).
[10] M. Gyulassy and X. N. Wang, Nucl. Phys. **B420**, 583 (1994).
[11] B. L. Combridge, Nucl. Phys. **B151**, 429 (1979).
[12] J. C. Collins, D. E. Soper, and G. Sterman, Nucl. Phys. **B263**, 37 (1986).
[13] R. K. Ellis, Report No. FERMILAB-CONF-86/35-T, 1986.
[14] E. Hoffmann and R. Moore, Z. Phys. C **20**, 71 (1983).
[15] G. Ingelman, L. Jönsson, and M. Nyberg, Phys. Rev. D **47**, 4872 (1993).
[16] R. Vogt, S. J. Brodsky, and P. Hoyer, Nucl. Phys. **B383**, 643 (1992).
[17] S. J. Brodsky, P. Hoyer, A. H. Mueller, and W. K. Tang, Nucl. Phys. **B369**, 519 (1992).
[18] M. Glück, E. Reya, and A. Vogt, Z. Phys. C **48**, 471 (1990).
[19] D. W. Duke and J. F. Owens, Phys. Rev. D **30**, 49 (1984).
[20] P. Nason, S. Dawson, and R. K. Ellis, Nucl. Phys. **B303**, 607 (1988); **B327**, 49 (1989).
[21] W. Beenakker, H. Kuijf, W. L. van Neerven, and J. Smith, Phys. Rev. D **40**, 54 (1989); W. Beenakker, W. L. van Neerven, R. Meng, G. Schuler, and J. Smith, Nucl. Phys. **B351**, 507 (1991).
[22] E. L. Berger, in Proceedings of the Advanced Workshop on QCD Hard Processes, St. Croix, 1988 (unpublished).
[23] E. L. Berger and R. Meng, Phys. Rev. D **46**, 169 (1992).
[24] I. Sarcevic and P. Valerio, Phys. Lett. B **338**, 426 (1994).
[25] S. Aoki *et al.*, Phys. Lett. B **224**, 441 (1989).
[26] A. T. Goshaw, in Proceedings of the Advanced Workshop on QCD Hard Processes, St. Croix, 1988 (unpublished).
[27] M. Aguilar-Benitez *et al.*, Phys. Lett. B **189**, 476 (1987).
[28] R. Ammar *et al.*, Phys. Rev. Lett. **61**, 2185 (1988).
[29] K. Kodama *et al.*, Phys. Lett. B **263**, 573 (1991).
[30] M. J. Leitch *et al.*, Phys. Rev. Lett. **72**, 2542 (1994).
[31] S. P. K. Tavernier, Rep. Prog. Phys. **50**, 1439 (1987).
[32] K. Goulianos, in *Physics Simulations at High Energies*, edited by V. Barger *et al.* (World Scientific, Singapore, 1987).
[33] H. Cobbaert *et al.*, Phys. Lett. B **206**, 546 (1987); M. E. Duffy *et al.*, Phys. Rev. Lett. **55**, 1816 (1985).
[34] UA1 Collaboration, C. Albajar *et al.*, Phys. Lett. B **256**, 121 (1991).
[35] L. Combridge, J. Kripfganz, and J. Ranft, Phys. Lett. **70**, 234 (1977).
[36] K. J. Eskola, Nucl. Phys. **B400**, 240 (1993).